Research Article | Vol. 34, No. 1 / 12 Jan 2026 / Optics Express 990

Optics EXPRESS

Dual-band dual-circularly polarized and orbital angular momentum multiplexed reflectarray

YUHUI REN,[1,4,†] YUTIAN MA,[1,5,†] KEJUAN LI,[2] LEHU WEN,[3] BOHANG ZHANG,[1] MINGYANG GAO,[1] WU ZHAO,[1] AND HANDONG WU[2]

[1] *School of Electronic Information, Northwest University, Xi'an 710127, China*
[2] *Xi'an HengDa Microwave Technology Development Co., Ltd., Xi'an 710100, China*
[3] *Department of Electronic and Electrical Engineering, Brunel University London, Uxbridge UB8 3PH, UK*
[4] *ryhui13579@163.com*
[5] *myt_nwu@163.com*
[†] These authors contributed equally.

Abstract: In this letter, a dual-band dual-circularly polarized (CP) orbital angular momentum (OAM) multiplexed reflectarray (RA) is proposed, capable of generating vortex electromagnetic beams with distinct polarizations, mode numbers (l), and radiation directions across different bands. First, it presents an innovative approach to achieving dual-band dual-CP decoupling. Second, the proposed RA integrates multiple multiplexing techniques, including frequency, polarization, and OAM. Specifically, a low-profile metasurface unit cell is designed, utilizing only a dielectric substrate and a metal patch, achieving a bandwidth ranging from 10.6 GHz to 18.1 GHz (52.2%). Furthermore, an RA constructed from these units fulfills the duplex communication requirements of Ku-band satellite systems. It generates a left-handed CP OAM beam with l=+1 in the downlink band (10.7-12.75 GHz), and a right-handed CP beam with l = -2 in the uplink band (12.75-18.1 GHz), with each beam exhibiting a distinct radiation direction.

1. Introduction

Metasurfaces, as two-dimensional artificial structures composed of subwavelength elements, have provided an unprecedented platform for controlling electromagnetic (EM) waves. Through precise manipulation of amplitude, phase, and polarization, metasurfaces have enabled compact and multifunctional optical devices for beam steering, focusing, holography, and polarization conversion [1–4]. Compared with conventional bulky optical components, metasurfaces exhibit the advantages of ultra-thin profiles, low loss, and easy integration, offering a promising route toward miniaturized and high-performance photonic systems. Owing to their flexibility in wavefront engineering, metasurfaces have also been widely explored in wireless communications, imaging, sensing, and information processing [5–10].

With the development of 5G-Advanced and 6G, the International Telecommunication Union (ITU) states that integrated satellite-terrestrial networks must achieve a peak data rate of at least 1 Tbps, posing unprecedented challenges to current communication technologies [11]. To address this challenge, researchers have proposed a range of multiplexing techniques, including frequency division multiplexing, polarization multiplexing, and orbital angular momentum (OAM) mode multiplexing [12–18]. Polarization multiplexing encompasses both linear polarization (LP) and circular polarization techniques. Notably, circularly polarized (CP) waves demonstrate superior performance in mitigating multipath interference and the Faraday rotation effect. Consequently, dual circularly polarized reflectarrays (dual-CP RAs) have emerged as a focal research area in satellite communication systems (SCS) [19–30]. Currently, the primary approach to achieving dual-CP multiplexing is the dual-CP decoupling technique introduced in 2020 [21]. Nevertheless, the metasurface proposed in that study exhibits a relatively narrow operational bandwidth. In

#582828 https://doi.org/10.1364/OE.582828
Journal © 2026 Received 29 Oct 2025; revised 17 Dec 2025; accepted 22 Dec 2025; published 7 Jan 2026

2023, Dai et al. proposed a dual-CP RA operating using a multi-parameter optimization strategy [30]. The design demonstrated notable improvements in both antenna bandwidth and aperture efficiency (AE), reaching 32.8% and 45.7%, respectively. Unfortunately, all of the aforementioned studies have only achieved single-band dual-CP decoupling, meaning that the proposed RAs operate within a single frequency band. Considering that modern SCS typically operate in a dual-band duplex mode—for instance, in Ku-band systems, where the downlink band spans 10.7 GHz to 12.75 GHz and the uplink band ranges from 12.75 GHz to 18.1 GHz—developing the reflectarray (RA) capable of dual-band dual-CP multiplexing is of considerable practical significance. The core technical challenge resides in achieving independent decoupling of dual-CP beams across two distinct frequency bands, i.e., realizing dual-band dual-CP decoupling.

Dual-band dual-CP RAs can be categorized into multi-layer and single-layer structural configurations. In multi-layer designs, individual layers target distinct EM wave bands [31–33]. While frequency selective surfaces (FSS) are often inserted to reduce inter-layer coupling, this approach tends to increase both structural thickness and insertion loss. Single-layer RAs are categorized into continuous [34–37] and discrete [38,39] phase control. Continuous designs integrate multi-frequency metasurface cells but suffer from mutual coupling and limited bandwidth. Discrete methods reduce coupling at the cost of aperture efficiency (AE) due to phase quantization.

In addition, vortex EM waves carrying OAM exhibit a helical phase front and intrinsic modal orthogonality, enabling theoretically infinite parallel transmission channels. To enhance spectral efficiency and data rates, a reflectarray (RA) scheme integrating dual-band dual-CP/LP multiplexing with OAM has been proposed [40–49]. The core challenge is efficiently integrating OAM into a dual-band dual-CP high-gain beam for vortex wave generation. While [41] proposed a dual-LP OAM-RA, LP vortices are unsuitable for SCS. Although [42] achieved a dual-CP design using a multi-layer structure (three dielectrics, five metals), it suffers from high complexity and profile.

In response to the above challenges, this letter proposes a dual-band dual-CP decoupling method by integrating the Berry phase (P_B) and dynamic phase (P_D) modulation mechanisms of the metasurface. A dual-band dual-CP multiplexing RA is successfully realized using only a single-layer dielectric substrate. Based on this, vortex beam forming was subsequently implemented, leading to the design of a dual-band dual-CP OAM-RA. As shown in Fig. 1, the proposed OAM-RA primarily consists of two components: a dual-CP feed and a metasurface. When a left-handed circularly polarized (LHCP) wave is incident, it is reflected by the metasurface to generate an LHCP vortex beam with a mode number of l_L and a null depth pointing to (φ_L, θ_L). Similarly, when a right-handed circularly polarized (RHCP) wave is incident, a RHCP vortex wave with a mode number of l_R and a null depth pointing to (φ_R, θ_R) is produced.

2. Theoretical basis of dual-band dual-CP decoupling

Reference [21] proposes a single-band dual-CP decoupling method achieved using only a single functional layer. The theory of single-band dual-CP decoupling is as follows.

As shown in Fig. 2, we take a hexagonal ring unit cell as an example for explanation. The incident electric field E_i can be decomposed into horizontal component (E_H) and vertical component (E_V). It is assumed that the electric fields of the LHCP and RHCP incident waves are represented by $\overrightarrow{E_L^i}$ and $\overrightarrow{E_R^i}$, respectively. The corresponding reflected electric fields are denoted as $\overrightarrow{E_L^r}$ and $\overrightarrow{E_R^r}$, and the relationship between the incident and reflected electric fields is expressed as:

$$\begin{aligned} \overrightarrow{E_L^r} &= \overrightarrow{E_L^i}\Gamma_{LL} + \overrightarrow{E_R^i}\Gamma_{LR} \\ \overrightarrow{E_R^r} &= \overrightarrow{E_R^i}\Gamma_{RR} + \overrightarrow{E_L^i}\Gamma_{RL} \end{aligned} \tag{1}$$

Optics EXPRESS

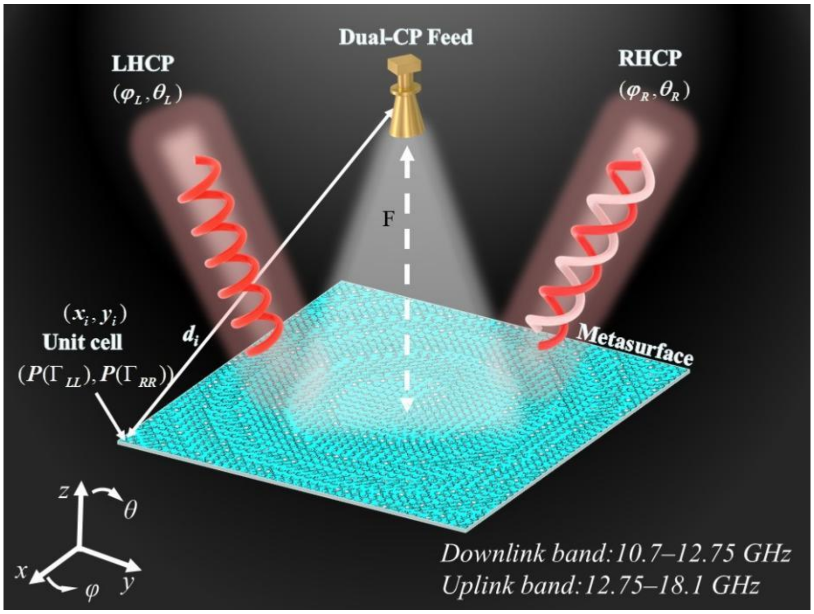

Fig. 1. Diagram of dual-band dual-CP OAM-RA.

Γ_{LL}, Γ_{RL} represent the co-polarization reflection coefficient and cross-polarization reflection coefficient of the unit for the LHCP wave, respectively; Γ_{RR}, Γ_{LR} represent the co-polarization reflection coefficient and cross-polarization reflection coefficient of the unit for the RHCP wave.

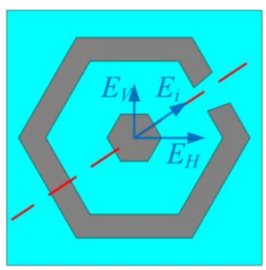

Fig. 2. Diagram of unit-line polarization incident.

For a well-performing reflectarray, considering that the magnitude of the co-polarization reflection coefficient is approximately equal to 1 and the cross-polarization reflection coefficient is approximately 0, the relationship between the reflection coefficients of the unit for circularly polarized waves and linearly polarized waves is as follows:

$$\begin{aligned} &\Gamma_{RR} = \Gamma_{HH} e^{j2a} = e^{j(P(\Gamma_{HH})+2a)} \\ &\Gamma_{LL} = \Gamma_{HH} e^{-j2a} = e^{j(P(\Gamma_{HH})-2a)} \\ &\Gamma_{LR} \approx 0 \\ &\Gamma_{RL} \approx 0 \end{aligned} \tag{2}$$

Γ_{HH}, Γ_{VV} represent the co-polarization reflection coefficients of the unit for horizontally and vertically polarized waves, respectively, $P(\Gamma_{HH})$ and $P(\Gamma_{VV})$ represent the corresponding reflection phases. a represents the rotation angle of the unit.

At this point, substituting equation (2) into equation (1) gives:

$$\begin{aligned}\overrightarrow{E_L^r} &= \overrightarrow{E_L^i} e^{j(P(\Gamma_{HH})-2a)}\\ \overrightarrow{E_R^r} &= \overrightarrow{E_R^i} e^{j(P(\Gamma_{HH})+2a)}\end{aligned} \tag{3}$$

Thus, the reflection phases of the unit for the LHCP wave and RHCP wave are respectively:

$$\begin{aligned}P(\Gamma_{LL}) &= P(\Gamma_{HH}) - 2a\\ P(\Gamma_{RR}) &= P(\Gamma_{HH}) + 2a\end{aligned} \tag{4}$$

In the specific design, $P(\Gamma_{HH})$ can correspond to the dynamic phase of the unit, and $2a$ ($-2a$) can correspond to the berry phase. That is, we obtain:

$$\begin{aligned}P(\Gamma_{LL}) &= P_D(\Gamma_{LL}) + P_B(\Gamma_{LL})\\ P(\Gamma_{RR}) &= P_D(\Gamma_{RR}) + P_B(\Gamma_{RR})\end{aligned} \tag{5}$$

To achieve single-band dual-CP decoupling, it is essential to ensure that the dynamic phase compensation for LHCP and RHCP waves on the metasurface is equal, while the Berry phase compensation is equal in magnitude but opposite in polarity. Specifically:

$$\begin{aligned}P_D(\Gamma_{RR}) &= P_D(\Gamma_{LL}) = P_D\\ P_B(\Gamma_{LL}) &= -P_B, P_B(\Gamma_{RR}) = P_B\end{aligned} \tag{6}$$

Therefore, equation (5) can be rewritten as:

$$\begin{aligned}P(\Gamma_{LL}) &= P_D - P_B\\ P(\Gamma_{RR}) &= P_D + P_B\end{aligned} \tag{7}$$

It can be concluded that the reflection phases of LHCP and RHCP waves on the metasurface can be effectively synthesized through the corresponding P_B and P_D.

However, in the design of the dual-band dual-CP RA, the phase compensation condition in Equation (6) requires modification, as follows:

$$\begin{aligned}&P_{D\_d}(\Gamma_{LL}) = P_{D\_u}(\Gamma_{RR}) = P_D\\ or\quad &P_{D\_u}(\Gamma_{LL}) = P_{D\_d}(\Gamma_{RR}) = P_D\end{aligned} \tag{8}$$

$$\begin{aligned}&P_{B\_d}(\Gamma_{LL}) = -P_B, P_{B\_u}(\Gamma_{RR}) = P_B\\ or\quad &P_{B\_u}(\Gamma_{LL}) = -P_B, P_{B\_d}(\Gamma_{RR}) = P_B\end{aligned} \tag{9}$$

where the subscript "u" denotes the uplink frequency band, while "d" denotes the downlink band.

At this stage, we have identified the three essential conditions to achieve dual-band dual-CP decoupling, as follow:

I. In the uplink and downlink frequency bands, the metasurface exhibits a co-polarized reflection coefficient of 1 and a cross-polarization reflection coefficient of 0, that is $|\Gamma_{LL}|$=$|\Gamma_{RR}|$=1, and $|\Gamma_{LR}|$=$|\Gamma_{RL}|$=0.

II. According to Equation (8), in the dual-frequency dual-CP RA, the P_D compensation for the LHCP wave in the downlink band must be equal to that for the RHCP wave in the uplink band, or vice versa. Additionally, the P_D must support a full 360° variation range.

III. From Equation (9), it is evident that in both the uplink and downlink bands, the metasurface provides P_B compensation of equal magnitude but opposite polarity for the LHCP and RHCP waves. Furthermore, the P_B is also capable of covering a full 360° variation range.

3. Dual-band dual-CP OAM reflectarray design and analysis

3.1. Unit cell design

Figure 3(a) illustrates the unit cell of metasurface designed in this study, which comprises a metal ground plane, a dielectric substrate, and a metal functional layer. The functional layer consists of a split hexagonal ring (SHR) and a smaller hexagonal patch arranged concentrically. This SHR essentially functions as a folded microstrip line. Adjusting its total length enables P_D compensation across a full 0° to 360° range. However, variations in the total length of the microstrip line may lead to frequency shifts, which significantly affect the operational bandwidth. Therefore, incorporating a small hexagonal patch at the center of the ring compensates for such frequency deviations. The metal functional layer is fabricated on a dielectric substrate F4B with a relative permittivity of 2.2 and a loss tangent below 0.001. An air gap between the substrate and the ground is introduced to enhance the working bandwidth. Additional geometric parameters are defined as $h_1 = 1.5$ mm, $h_2 = 1.6$ mm, and $d = 7.5$ mm.

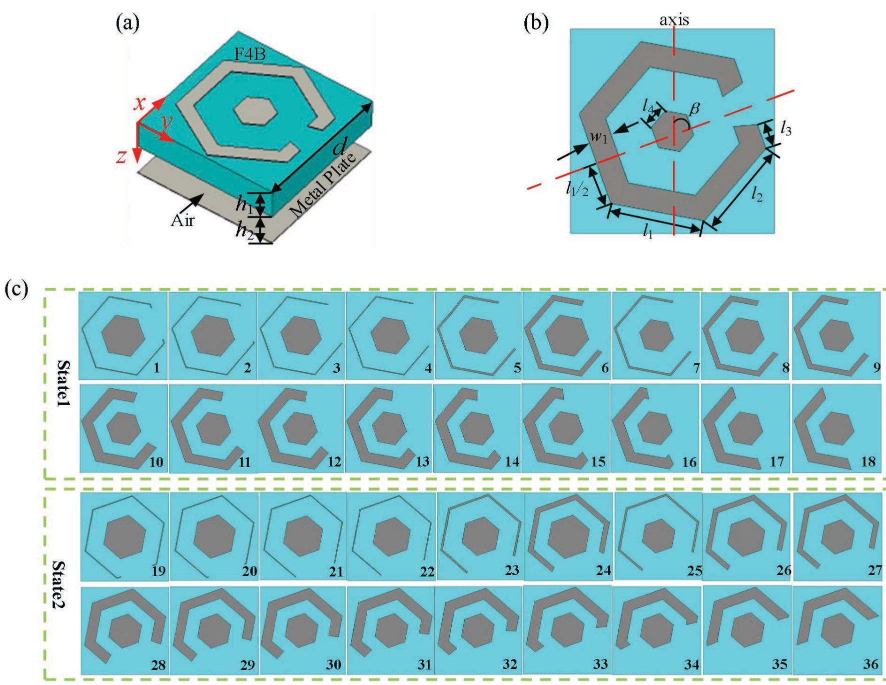

Fig. 3. (a) 3D view and (b) top view of the proposed metasurface unit; (c) the configuration of the 36-unit structure corresponds to different P_D states.

As illustrated in Fig. 3(b), the total length of the SHR can be mathematically expressed as: $l = (3l_1/2 + l_2 + l_3) \times 2$. By appropriately adjusting the parameters l, l_4, and w_1, it is possible to achieve arbitrary P_D compensation across the range of 0° to 360°. For the purpose of simplifying

Optics EXPRESS

the analysis, the continuous P_D variation over 360° is discretized, with two representative states defined for further analysis. In State 1, the direction angles of unit 1 through 18 are uniformly set to β, which corresponds to the angle between the direction of the SHR opening and its axis of symmetry. These eighteen unit cells with varying dimensions can collectively achieve a P_D coverage ranging from 0° to 170°, with a uniform phase step of 10°. By rotating all unit cells clockwise by 90°, State 2 is established, in which the directional angle is adjusted to $\beta + 90°$. The eighteen units in State 2 are labeled as units 19 to 36 and are capable of covering a P_D range from 180° to 350°. The configuration of the 36-unit is schematically illustrated in Fig. 3(c), while the detailed dimensional parameters of each unit cell are summarized in Table 1.

Table 1. Parameters of unit cells of metasurface (mm)

No.	1/19	2/20	3/21	4/22	5/23	6/24
DP(°)	0/180	10/190	20/200	30/210	40/220	50/230
l	18.6	18.2	18	17.3	17.1	16.5
w_1	0.1	0.1	0.1	0.1	0.2	0.5
l_4	1.9	1.9	1.8	1.7	1.7	1.5
No.	7/25	8/26	9/27	10/28	11/29	12/30
DP(°)	60/240	70/250	80/260	90/270	100/280	110/290
l	16.5	16	15.7	15.9	15.2	14.8
w_1	0.2	0.5	0.5	1	0.9	1
l_4	1.7	1.5	1.5	1.5	1.5	1.5
No.	13/31	14/32	15/33	16/34	17/35	18/36
DP(°)	120/300	130/310	140/320	150/330	160/340	170/350
l	14.2	13.6	13	12.2	11.4	11.1
w_1	1	1	1	1	1	1
l_4	1.5	1.5	1.5	1.5	1.5	1.5

Figure 4(a) and (b) present the simulated reflection coefficients of the metasurface unit under CP incident waves. Within the frequency range of 10.6 GHz to 18.1 GHz, $|\Gamma_{LL}|$ and $|\Gamma_{RR}|$ remain above -0.5 dB, while $|\Gamma_{LR}|$ and $|\Gamma_{RL}|$ stay below -10 dB. This demonstrates that the designed metasurface unit satisfies the Condition (I) for dual-band dual-CP decoupling. It is noted that, as shown in Table 1, the P_D modulation characteristics of corresponding units in States 1 and 2 are identical. For clarity and graphical simplicity, only the reflection coefficients of the nine units labeled with odd numbers in State 1 are displayed in the figure. These results were obtained from full-wave simulations performed in CST Microwave Studio.

Figure 4(c) and (d) show the reflection phase characteristics of each metasurface unit under CP incident waves. It is observed that the reflection phase of each unit varies approximately linearly within the frequency range of 10.6 GHz to 18.1 GHz. Taking Unit 1 and Unit 17 as examples, the reflection phase of Unit 1 for the LHCP wave at 11.725 GHz is 14.3°, while for the RHCP wave at 15.425 GHz, it is 12.73°, with both values being approximately equal. Similarly, Unit 17 exhibits reflection phases of 171.5° for the LHCP wave at 11.725 GHz and 173.2° for the RHCP wave at 15.425 GHz, which are also nearly identical. These results confirm that each unit satisfies Equation (8) for P_D compensation of LHCP and RHCP waves in the downlink and uplink bands. Simulation optimization further yields a value of $\beta = 70.5°$. Figure 4(e) presents the extracted $P_{D\text{–}d}(\Gamma_{\mathrm{LL}})$values at 11.725 GHz and $P_{D\text{–}u}(\Gamma_{\mathrm{RR}})$ values at 15.425 GHz for the 18 units in State 1. The two resulting curves are observed to be nearly identical, thereby further supporting the same conclusion. Accordingly, the proposed metasurface unit satisfies the Condition (II) for dual-band dual CP decoupling. Figure 4(f) illustrates the relationship between the rotation angle

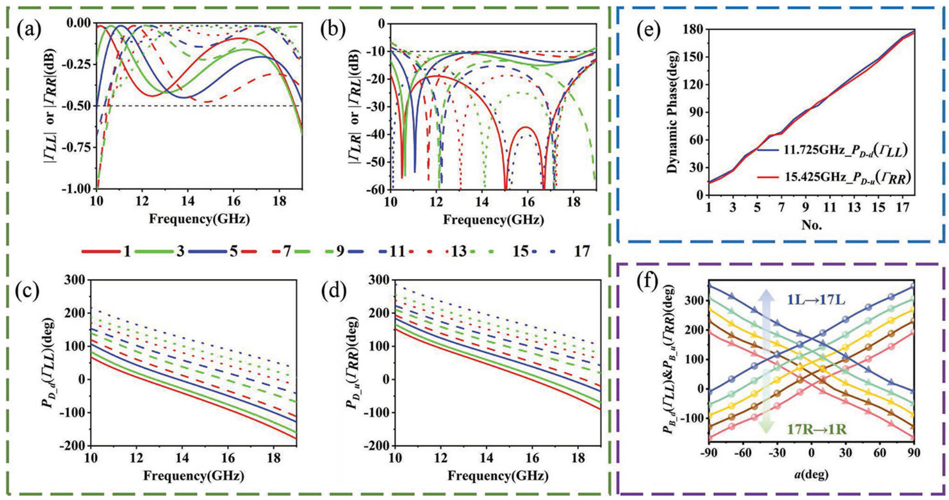

Fig. 4. The reflection coefficients of CP incident wave obtained by numerical calculation, (a) $|\Gamma_{\text{LL}}|$ or $|\Gamma_{\text{RR}}|$, (b) $|\Gamma_{\text{LR}}|$ or $|\Gamma_{\text{RL}}|$, (c) $P_{D-d}(\Gamma_{\text{LL}})$, (d) $P_{D-u}(\Gamma_{\text{RR}})$; (e) 11.725 GHz and 15.425 GHz P_D comparison; (f) P_B distribution of the metasurface unit.

α of the unit and the P_B. A total of five units (NO. 1, 5, 9, 13, and 17) from State 1 were selected as the subjects for analysis. In the downlink band (f = 11.725 GHz), as α varies gradually from -90° to 90°, the $P_{B-d}(\Gamma_{\text{LL}})$ decreases linearly from 0° to 360°. Specifically, a 1° rotation of α results in a 2° decrease in $P_{B-d}(\Gamma_{\text{LL}})$. In contrast, in the uplink band (f = 15.425 GHz), the $P_{B-u}(\Gamma_{\text{RR}})$ increases linearly with α, with a 1° rotation leading to a 2° increase in $P_{B-u}(\Gamma_{\text{RR}})$. These characteristics demonstrate that the designed metasurface unit fulfills Condition (III) for dual-band dual CP decoupling.

The aforementioned analysis of the unit's characteristics was limited to the scenario of normal EM wave incidence. However, in practical array configurations, most units experience non-normal incidence relative to the feed source. Therefore, it is essential to evaluate the performance of the unit under oblique incidence conditions.

In practical reflectarray designs, the maximum incident angle of the electromagnetic waves on the array edge elements is approximately 30°. Therefore, the range of oblique incident angles can be defined as 0° to 30°. For simplicity in analysis, the No. 6 unit cell from State 1 was selected at two frequency points, 11.725 GHz and 15.725 GHz. The oblique-incidence simulations were carried out using CST Microwave Studio.

The unit was rotated by 60° and 100° for oblique incidence performance simulation analysis. The simulation results of the reflection coefficient magnitude and phase variation with incident angle are shown in Fig. 5, indicating that as the oblique incident angle of the unit increases, the unit can still maintain a high reflection coefficient, with the polarization purity of the reflected wave remaining at a high level, and the reflection phase fluctuating minimally with the incident angle.

In summary, as the incident angle increases from 0° to 30°, the proposed unit maintains a high level of reflectivity and polarization purity, while exhibiting minimal variation in reflection phase with respect to the incident angle.

3.2. Reflectarray design

The design of the metasurface unit for dual-band dual-CP OAM-RA has now been completed, and the subsequent step is to form an array. As illustrated in Fig. 1, the length and width of the metasurface are both D = 300 mm, and it is composed of a 40 × 40 unit cell arrangement. The

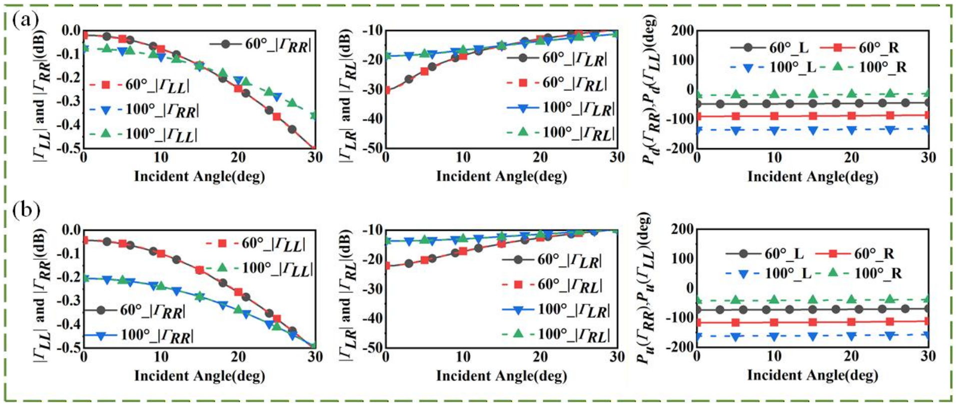

Fig. 5. Analysis of the Unit cell' s Oblique Incidence Performance(a)11.725 GHz (b)15.425 GHz.

reflectarray features a focal ratio (F/D) of approximately 0.866, corresponding to a focal length of 259.8 mm. The design of the dual-CP feed is detailed in Section S1 of the Supplement 1. With respect to the phase compensation required for each of the 1600 units on the array, the detailed calculation procedure is outlined as follows:

***Step* 1**: Calculate the theoretical phase compensation required for each unit cell based on the desired beam direction, which specifically satisfies the formula:

$$\begin{aligned} P_d(\Gamma_{LL}) &= k_0 \times [d_i - (x_i cos\varphi_L + y_i \sin\varphi_L) sin\theta_L] + l_L \times \arctan(y_i/x_i) \\ P_u(\Gamma_{RR}) &= k_0 \times [d_i - (x_i cos\varphi_R + y_i \sin\varphi_R) sin\theta_R] + l_R \times \arctan(y_i/x_i) \end{aligned} \quad (10)$$

where d_i denotes the distance from the feed the i-th unit, (x_i, y_i) represent the spatial coordinates of the i-th unit, l_L and l_R denote the mode numbers associated with the two vortex beams, respectively.

In this design, the desired pointing directions of the two vortex beams are specified as (φ_L, θ_L) =(90°,3°)and (φ_R, θ_R) =(-90°,-5°), with the corresponding mode numbers given by l_L =+1 and l_R = -2, respectively. Substituting these parameters into Equation (10) yields the values of $P_d(\Gamma_{\mathrm{LL}})$ and $P_u(\Gamma_{\mathrm{RR}})$, as illustrated in Fig. 6(a).The first two subfigures in Fig. 6(a) show the required phase distributions for generating the l=+1 and $l = -2$ OAM beams. These phase distributions were obtained using a MATLAB-based numerical implementation of the theoretical phase-compensation expressions in Eq. (10). For the LHCP case, the phase increases counterclockwise by 2π, while for the RHCP case it decreases clockwise by 4π, corresponding to one and two helical rotations, respectively. These phase-winding behaviors directly visualize the designed OAM modes.

***Step* 2**: Based on Equation (7), $P_d(\Gamma_{\mathrm{LL}})$ and $P_u(\Gamma_{\mathrm{RR}})$ are decomposed into their respective P_D and P_B components associated with each unit cell. The corresponding computational results are also displayed in Fig. 6(a). The last two subfigures in Fig. 6(a) present the dynamic phase and Berry phase components obtained from Eq. (7). Together, these components enable the metasurface to realize the required dual-band OAM phase profiles.

***Step* 3**: Determine the dimensional parameters and rotational angles for each unit. Once the P_D of each unit is determined, the corresponding dimensional dimensions can be retrieved from Table 1. As illustrated in Fig. 4(f), a distinct relationship exists between the unit's rotation angle α and its P_B. Specifically, $\alpha = P_B$ /2.

***Step* 4**: Once the size parameters and rotation angles of each unit have been determined, the array modeling process can proceed accordingly.

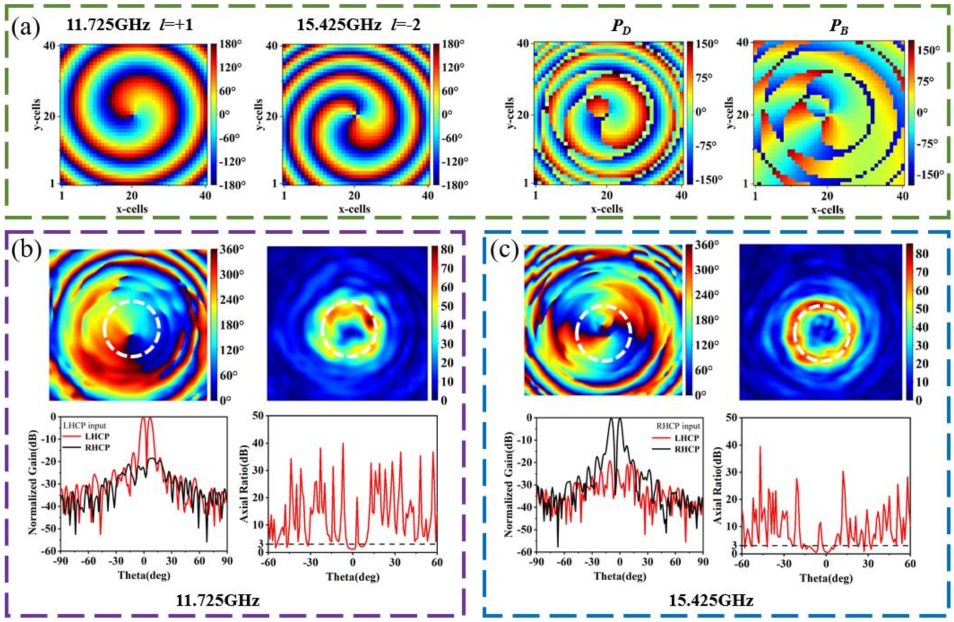

Fig. 6. (a) The OAM phase, P_D and P_B corresponding to each unit in the array; Simulation results at the frequency of (b)11.725 GHz and (c)15.425 GHz.

3.3. Simulation results and discussions

Figure 6(b) and (c) show the simulation results of the proposed dual-band dual-CP OAM-RA when an 11.725 GHz LHCP wave is incident and when a 15.425 GHz RHCP wave is incident. These full-array electromagnetic simulations were carried out using CST Microwave Studio with an open (radiation) boundary and a horn-feed excitation model. From the figures, it can be seen that at 11.725 GHz, the zero zone of the vortex beam points to (φ_L, θ_L) =(90°,3°), the divergence angle is 7.7°, and the main mode of the vortex wave is +1. For the incidence of the RHCP at 15.425 GHz, the zero zone of the vortex beam points to (φ_R, θ_R) =(-90°,-5°), the divergence angle measures 9.1°, and the main mode is identified as -2, all of which align well with the initial design objectives.

3.4. Experiment results

To further validate the effectiveness of the proposed method, the dual-band dual-CP OAM-RA was fabricated and experimentally tested. Figures 7(a) and (c) present a photograph of the fabricated prototype along with the testing setup in a microwave anechoic chamber. Considering the requirement to measure the phase characteristics of the vortex wave, planar near-field scanning was employed. The sampling plane was positioned at a distance of 600 mm from the OAM-RA, with a scanning area of 400 mm × 400 mm.

Figures 7(b) and (d) present the normalized radiation patterns as well as the electric field phase distribution at the center frequency obtained from the experimental measurements. As observed from the figures, the beam pointing directions at all frequency points align well with the simulation results. However, factors such as fabrication tolerances and measurement inaccuracies result in a reduction in antenna gain and OAM purity. Specifically, at 11.725 GHz, the purity of the +1 mode vortex wave is measured as 0.9, while at 15.425 GHz, the purity of the -2 mode vortex wave is 0.81. Additional simulation and measurement results are summarized in Table 2.

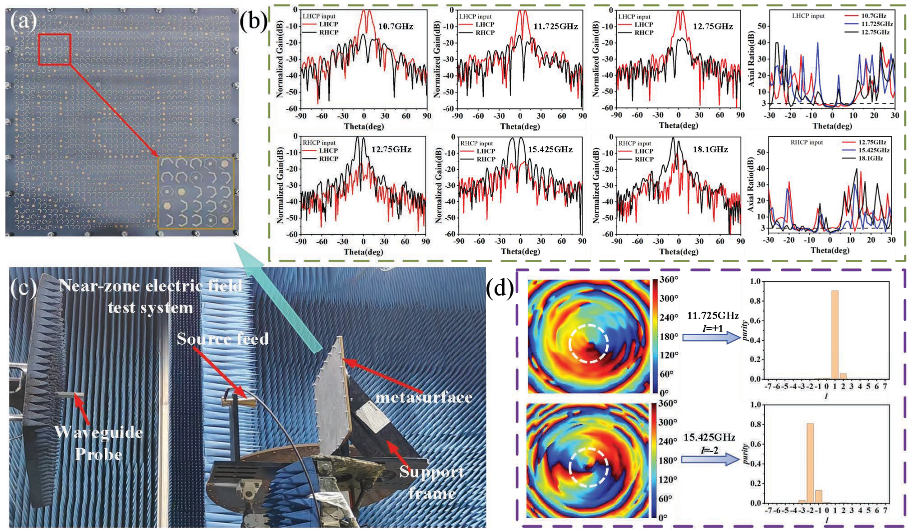

Fig. 7. (a) The graph of the proposed OAM-RA; (b)Measured radiation pattern and axial ratio of the OAM-RA; (c)The test scenario of the OAM-RA; (d)The electric field phase distribution and purity of the OAM-RA.

Table 2. Summary of Radiation Characteristics for the Proposed OAM-RA

Polar.	Mode	Freq. (GHz)		Gain (dBic)		NDP (°)[a]		Div. angle (°)		Purity	
				Sim.	Mea.	Sim.	Mea.	Sim.	Mea.	Sim.	Mea.
			10.7	21.8	21.27	4	5	8.7	8	0.93	0.85
LHCP	+1	downlink	11.725	23.8	22.52	3	3	7.7	7	0.95	0.9
			12.75	24.3	23.61	3	4	6.7	6.5	0.91	0.83
			12.75	19.2	19.05	-6	-7	12.7	12	0.8	0.75
RHCP	-2	up link	15.425	25.1	24.89	-5	-5	9.1	9	0.87	0.81
			18.1	23.9	23.33	-3	-4	7.93	7	0.75	0.7

[a]NDP: null depth pointing

Table 3 presents a comparative analysis of the performance between the proposed dual-band dual-CP OAM-RA and previous OAM-RA designs. Most existing OAM-RA designs support only dual-linear polarization, or achieve only single-band dual-CP OAM generation. Some recent dual-band dual-CP approaches rely on multi-layer structures or multiple patch types, which inevitably increase structural complexity and reduce scalability.

In contrast, the proposed OAM-RA achieves dual-band dual-CP OAM generation using only a single dielectric substrate and a single patch configuration, while simultaneously providing effective polarization decoupling. This compact implementation offers clear advantages in fabrication simplicity, integration feasibility, and overall system efficiency, and therefore represents a competitive solution compared with current metasurface-based OAM RA.

4. Conclusion

Inspired by the single-band dual-CP decoupling method, we have developed and implemented a dual-band dual-CP decoupling approach tailored to the application requirements of full-duplex SCS. Based on this approach, a dual-band dual-CP OAM-RA covering both the Ku-band uplink and downlink has been designed. Full-wave simulations and experimental validations confirm the

Optics EXPRESS

effectiveness of this approach, which integrates frequency, polarization, and OAM multiplexing to enhance spectral efficiency for next-generation communication systems.

Table 3. Comparisions with other OAM-RAs

Ref.	Num. of Fre.	Num. of substrate	Num. of patch	Polar.	P-D[a]
[40]	1	1	1	Dual-LP	Yes
[41]	2	1	1	Dual-LP	Yes
[42]	2	3	5	Dual-CP	Yes
[43]	2	1	1	LHCP	No
[44]	2	1	1	Y-LP + LHCP	Yes
[45]	1	1	1	Dual-CP	Yes
[46]	2	3	5	Dual-CP	Yes
[47]	1	1	1	Dual-LP	No
[48]	2	1	1	Dual-LP	No
[49]	2	3	3	Dual-CP	Yes
This work	2	1	1	Dual-CP	Yes

[a]P-D: Polarization decoupling

See the Supplement 1 for the analysis of the design of source feed.

Funding. Key Research and Development Program of Shaanxi (2024GX-ZDCYL-01-29); Key Research and Development Program of Xianyang city (L2025-ZDYF-KTH-006).

Disclosures. The authors declare no conflicts of interest.

Data availability. The data that support the findings of this study are available from the corresponding authors upon reasonable request.

Supplemental document. See Supplement 1 for supporting content.

Reference

1. D. Lin, P. Fan, E. Hasman, *et al.*, "Dielectric gradient metasurface optical elements," Science **345**(6194), 298–302 (2014).
2. A. Arbabi, E. Arbabi, Y. Horie, *et al.*, "Planar metasurface retroreflector," Nat. Photonics **11**(7), 415–420 (2017).
3. H. Li, T. Nan, W. Xu, *et al.*, "Single-layer multiplexed metasurfaces with on-demand polarization encoding based on a symmetric Jones matrix," Opt. Express **33**(3), 5445–5459 (2025).
4. Z. Wang, Y. Yao, W. Pan, *et al.*, "Bifunctional manipulation of terahertz waves with high-efficiency transmissive dielectric metasurfaces," Adv. Sci. **10**(4), 2205499 (2023).
5. Y. Fu, Y. Li, X. Fu, *et al.*, "A dual-broadband liquid-crystal programmable metasurface and its application in terahertz wireless communications," Engineering, (2025).
6. W. Li, F. Li, W. Tang, *et al.*, "Stretchable antenna arrays-enabled multi-target balloon wireless communication system," Adv. Funct. Mater. **35**, e10521 (2025).
7. W. Tang, S. Meng, Q. Y. Zhou, *et al.*, "Real-time wireless sensing and positioning through reconfigurable intelligent surfaces," IEEE Trans. Wireless Commun. (2025).
8. R. Fu, K. Chen, Z. Li, *et al.*, "Metasurface-based nanoprinting: principle, design and advances," Opto-Electron. Sci. **1**(10), 220011 (2022).
9. M. Rossi, L. Zhang, X. Q. Chen, *et al.*, "Machine-learning-enabled multi-frequency synthesis of space-time-coding digital metasurfaces," Adv. Funct. Mater. **34**(40), 2403577 (2024).
10. H. Wu, R. Shao, Z. Xu, *et al.*, "A programmable metasurface antenna that approaches the wireless information mapping limit," Nat. Electron. **8**(2), 179–191 (2025).
11. ITU-R, "Framework and overall objectives of the future development of IMT for 2030 and beyond," ITU-R M.[IMT-2030] (2023).
12. K. Zhang, Y. Wang, S. N. Burokur, *et al.*, "Generating dual-polarized vortex beam by detour phase: From phase gradient metasurfaces to metagratings," IEEE Trans. Microw. Theory Techn. **70**(1), 200–209 (2022).
13. Y. Yan, G. Xie, M. P. J. Lavery, *et al.*, "High-capacity millimetre-wave communications with orbital angular momentum multiplexing," Nat. Commun. **5**(1), 4876 (2014).
14. Y. Chen, S. Zheng, X. Jin, *et al.*, "Single-frequency computational imaging using OAM-carrying electromagnetic wave," J. Appl. Phys. **121**(18), 184506 (2017).

Optics EXPRESS

15. Z. Huang, Y. He, P. Wang, *et al.*, "Orbital angular momentum deep multiplexing holography via an optical diffractive neural network," Opt. Express **30**(4), 5569–5584 (2022).
16. Y. Li and K. Luk, "A low-divergence circularly polarized dual-mode OAM antenna based on higher order Laguerre–Gaussian modes," IEEE Trans. Antennas Propag. **69**(9), 5215–5223 (2021).
17. T. Zhang, J. Liu, Z. Lin, *et al.*, "A compact multimode OAM antenna using sequentially rotated configuration," Antennas Wirel. Propag. Lett. **21**(1), 134–138 (2022).
18. J. Lin, H. Zhao, H. Lu, *et al.*, "Generating the dual-band and multimode OAM by irregular pentagonal patch antenna array," Electron. Lett. **56**(10), 476–478 (2020).
19. S. Mener, R. Gillard, R. Sauleau, *et al.*, "Dual circularly polarized reflectarray with independent control of polarizations," IEEE Trans. Antennas Propag. **63**(4), 1877–1881 (2015).
20. W.-L. Guo, F. Yuan, H.-X. Xu, *et al.*, "Broadband spin-decoupled meta-devices enabled by a polarization conversion metasurface," Antennas Wirel. Propag. Lett. **23**(3), 920–924 (2024).
21. Z. H. Jiang, T. Yue, W. Hong, *et al.*, "Low-profile and wideband dual-circularly polarized reflect-arrays based on rotated metal-backed dual-polarized aperture-coupled patch elements," IEEE Trans. Antennas Propag. **68**(3), 2108–2117 (2020).
22. Y. Li, Z. H. Jiang, X. F. Tong, *et al.*, "Wideband dual-circularly-polarized reflect-arrays based on dual-functional-layer cells with Berry-phase compensation at X-band," IEEE Trans. Antennas Propag. **70**(10), 9924–9929 (2022).
23. C. S. Geaney, M. Hosseini, S. V. Hum, *et al.*, "Reflectarray antennas for independent dual linear and circular polarization control," IEEE Trans. Antennas Propag. **67**(9), 5908–5918 (2019).
24. Z. H. Jiang, Y. Zhang, W. Hong, *et al.*, "Anisotropic impedance surface enabled low-profile broadband dual-circularly polarized multibeam reflectarrays for Ka-band applications," IEEE Trans. Antennas Propag. **68**(8), 6441–6446 (2020).
25. W. L. Guo, G. M. Wang, W. Y. Ji, *et al.*, "Broadband spin-decoupled metasurface for dual-circularly polarized reflector antenna design," IEEE Trans. Antennas Propag. **68**(5), 3534–3543 (2020).
26. X. Zhang, F. Yang, S. Xu, *et al.*, "Single-layer reflectarray antenna with independent dual-CP beam control," Antennas Wirel. Propag. Lett. **19**(4), 532–536 (2020).
27. J. Yin, Q. Lou, H. Wang, *et al.*, "Broadband dual-polarized single-layer reflectarray antenna with independently controllable 1-bit dual beams," IEEE Trans. Antennas Propag. **69**(6), 3294–3302 (2021).
28. L. X. Wu, Q. Hu, X. Y. Luo, *et al.*, "Wideband dual-feed dual-polarized reflectarray antenna using anisotropic metasurface," Antennas Wirel. Propag. Lett. **21**(1), 129–133 (2022).
29. H. X. Xu, S. Wang, C. Wang, *et al.*, "Polarization-insensitive metalens and its applications to reflectarrays with polarization diversity," IEEE Trans. Antennas Propag. **70**(3), 1895–1905 (2022).
30. X. W. Dai, Y. H. Zhang, W. Yu, *et al.*, "A broadband low-profile dual-circularly polarized reflect-array based on a single-layer microstrip patch for Ka-band application," IEEE Trans. Antennas Propag. **71**(6), 4932–4940 (2023).
31. I. Derafshi, N. Komjani, E. Ghasemi, *et al.*, "Dual-band X/Ku reflectarray antenna using a novel FSS-backed unit-cell with quasi-spiral phase delay line," J. Microw. Optoelectron. Electromagn. Appl. **15**(3), 225–236 (2016).
32. R. Y. Deng, F. Yang, S. Xu, *et al.*, "An FSS-backed 20/30-GHz dual-band circularly polarized reflectarray with suppressed mutual coupling and enhanced performance," IEEE Trans. Antennas Propag. **65**(2), 926–931 (2017).
33. P. Xu, R. Li, H. Liu, *et al.*, "Dual-circularly polarized spin-decoupled reflectarray with FSS-back for independent operating at Ku-/Ka-bands," IEEE Trans. Antennas Propag. **69**(10), 7041–7046 (2021).
34. R. S. Malfajani, B. A. Arand, W. Zhang, *et al.*, "Dual-band orthogonally polarized single-layer reflectarray antenna," IEEE Trans. Antennas Propag. **65**(11), 6145–6150 (2017).
35. F. Xue, H. Wang, M. Yi, *et al.*, "Design of X/Ku dual-band dual-linear polarization reflectarray using double parallel dipole elements," Prog. Electromagn. Res. C **66**, 11–20 (2016).
36. R. Deng, Y. L. Mao, S. Xu, *et al.*, "A single-layer dual-band circularly polarized reflectarray with high aperture efficiency," IEEE Trans. Antennas Propag. **63**(7), 3317–3320 (2015).
37. X. Tong, Z. H. Jiang, Y. Li, *et al.*, "Dual-wideband dual-circularly-polarized shared-aperture reflectarrays with a single functional substrate for K-/Ka-band applications," IEEE Trans. Antennas Propag. **70**(7), 5404–5417 (2022).
38. P. Xu, H. Liu, R. Li, *et al.*, "Ultrathin single-layer dual-band dual-circularly polarized reflectarray for K-/Ka-band satellite communications," IEEE Trans. Antennas Propag. **72**(9), 7122–7134 (2024).
39. P. Xu, M. Liu, X. Luo, *et al.*, "Single-layer polarization-insensitive dual-band reflectarray," Antennas Wirel. Propag. Lett. **24**(3), 646–650 (2025).
40. H. Yang, S. L. Zheng, H. Q. Zhang, *et al.*, "A reflective metasurface for OAM and polarization multiplexing communication in the W-band," Antennas Wirel. Propag. Lett. **23**(3), 1124–1128 (2024).
41. Y. Jiang, S. Li, X. Chen, *et al.*, "Frequency-polarization multiplexing reflective metasurface for orbital angular momentum generation," Appl. Phys. Lett. **124**(22), 221701 (2024).
42. P. Xu, H. Liu, R. Li, *et al.*, "Dual-band spin-decoupled metasurface for generating multiple coaxial OAM beams," IEEE Trans. Antennas Propag. **70**(11), 10678–10690 (2022).
43. J. Lin, C. Chen, J. Ding, *et al.*, "Dual-frequency multiple compact vortex beams generation based on single-layer bi-spectral metasurface," Appl. Phys. Lett. **119**(8), 081905 (2021).
44. J. Chen, J. Song, C. Huang, *et al.*, "Dual-band vortex beam generation with different OAM modes using single-layer metasurface," Opt. Express **27**(1), 34–44 (2019).

45. F. Li, X. Yin, and J. Deng, "Wideband reflective metasurface for independent control of mode and circular polarization of orbital angular momentum," Opt. Express **31**(26), 43975–43988 (2023).
46. P. Xu, K. Zhang, H. Liu, *et al.*, "Dual-band metasurface generating multiple OAM beams independently in full polarizations," Opt. Express **31**(20), 32637–32651 (2023).
47. N. Li, S. Zheng, H. Yang, *et al.*, "A broadband dual-polarized reflective metasurface for THz OAM communication," IEEE Trans. Microw. Theory Techn. **72**(2), 1302–1311 (2024).
48. S. Li and J. Cui, "Dual-Band Shared-Aperture Multimode OAM-Multiplexing Antenna Based on Reflective Metasurface," Phys. Sci. Forum **10**(1), 6 (2024).
49. Y. Zhang, T. Wu, Y. Zhou, *et al.*, "Dual-frequency broadband metasurface for independently generating multiple vortex beams based on spin decoupling," Opt. Mater. Express **15**(10), 2349–2361 (2025).